Check for updates

Influence of disk aberrations on high-power thin-disk laser cavities

MORITZ SEIDEL,[1,2,*] [iD] LUKAS LANG,[1,2] [iD] CHRISTOPHER R. PHILLIPS,[1] [iD] AND URSULA KELLER[1] [iD]

[1]*Institute for Quantum Electronics, ETH Zurich, 8093 Zurich, Switzerland*
[2]*These authors contributed equally to this work*
[*]*seidelm@phys.ethz.ch*

Abstract: We present a systematic study on the influence of thin-disk aberrations on the performance of thin-disk laser oscillators. To evaluate these effects, we have developed a spatially resolved numerical model supporting arbitrary phase profiles on the intracavity components that estimates the intracavity beam shape and the output power of thin-disk laser oscillators. By combining this model with the experimentally determined phase profile of the thin-disk (measured with interferometry), we can predict the operation mode of high-power thin-disk lasers, including mode degradation, higher-order mode coupling, and stability zone shrinking, all of which are in good agreement with experiment. Our results show that one of the main mechanisms limiting the performance is the small deviation of the disk's phase profile from perfect radial symmetry. This result is an important step to scaling modelocked thin-disk oscillators to the kW-level and will be important in the design of future active multi-pass cavity arrangements.

1. Introduction

High-average-power continuous-wave (cw) and ultrafast laser sources find many applications in research and industry, such as extreme ultraviolet light generation and micromachining [1–3]. The high average powers required for these applications are commonly achieved in systems based on the slab [4], fiber [5] or thin-disk laser (TDL) [6] gain geometries. In the MOPA (master oscillator power amplifier) architecture, the thin-disk laser system has been demonstrated with up to 10 kW output power in cw [7] and up to 2 kW in ultrafast [8] operation. However, due to the complexity inherent to MOPAs, it is very appealing to consider the power scaling of the laser oscillator itself [9,10]. Currently, the highest average power oscillators providing near diffraction limited beam quality achieve up to 4 kW in cw [11] and 350 W in modelocked [12] operation. Both results were achieved using the thin-disk gain geometry, which enables power-scaling by simultaneously increasing the pump and laser mode radius on this thin-disk while keeping the ratio of the two constant; empirically, the optimal ratio between pump and laser has been found to be around 70-80%.

For modelocking of thin-disk lasers, it is generally understood that higher-order mode operation should be avoided [9]. Such modes can be excited due to aberrations and resonances [13,14], and thus it is important to investigate the factors affecting beam quality in these lasers more closely. It is well known that one of the key considerations when designing thin-disk cavities is the influence of the thermal lens of the disk on the cavity mode evolution. The thermal lensing effects of the disk can be explained via a temperature dependent radius of curvature in combination with heating and convection of the gas in front of the disk [15]. To model such parabolic phase profiles, the ray transfer matrix formalism [16] for Gaussian beam propagation is typically used. Within this theory, cavities with larger beams can generally tolerate a smaller range of thermal lens values (as measured in diopters) before becoming unstable [17]. The working-point dependent thermal lens of the disk is usually included in the design so that the cavity is optimized for operation at full power. However, non-parabolic terms are not accounted for within the ray transfer matrix

theory and were previously neglected [18]. Therefore, alternative models are needed in order to account for beam quality degradation in cavities that are predicted by conventional models to be nominally stable. For example, nominally stable cavities with an appropriate ratio between the laser and pump spot sizes are shown to exhibit distorted mode operation, which could not be predicted before.

More detailed analyses of the thermal lensing including finite element simulations have been performed in the past, but only account for rotationally symmetric aberrations of the thin-disk [19]. A simulation model focusing on reproducing intensity profiles from thin-disk multipass amplifiers has been implemented [20], but only includes symmetric aspheric components of the disk and does not capture the influence of varying higher-order aberration across the pump spot.

A numerical investigation into the natural convection close to the surface of the disk distortion has previously been carried out [21,22] and also been expanded to include the gas-lens effect in front on the thin-disk [15]. Convection breaks the radial symmetry, resulting in a linear contribution to the phase (in addition to the lensing effects), corresponding to a beam deflection. However, other types of non-parabolic and non-radially-symmetric aberrations on the thin-disk have received little attention. Here, we show experimental evidence that suggests that these aberrations are crucial for the final performance of TDL cavities. The same effects might also explain previous observations of distorted fundamental mode operation and beam quality degradation in oscillators as well as amplifiers [7,12,23,24].

To quantify the influences of these effects and understand issues limiting the power scaling of many TDLs even if the cavity is designed for an optimal pump to laser spot size ratio, we present here a spatially resolved model of the laser oscillator. This model supports arbitrary phase profiles and gain distributions which, to the best of our knowledge, has not been demonstrated before for TDL oscillator simulations. The simulations use experimentally measured phase profiles, which is critical to obtain realistic predictions. The results of these simulation show good agreement with experiments in a standard high-power thin-disk laser cavity and are an important step to scaling cw and modelocked TDLs towards the next power milestones as thermal effects increase for larger laser spot sizes in the gain medium.

Our results should benefit a variety of high-power laser development efforts. For example, in active multi-pass arrangements (where the laser passes the disk several times during a cavity roundtrip), disk aberrations are sampled multiple times and with potentially different beam profiles on each pass, making prediction of the mode degradation effects particularly challenging without our new model. Another promising approach to achieve fundamental mode operation of a high-power TDL oscillator over a wide tuning range was recently demonstrated by using an intracavity spherically deformable mirror [24,25]. The results presented here suggest, that non-spherically deformable mirrors can be beneficial to improve the performance of TDL further, and simulations could guide the design of the required phase profile. Finally, our model can be applied easily to amplifiers as well as oscillator architectures

In section 2 we present the experimental setups, which includes the thin-disk laser cavity itself and the interferometer used to measure the disk. In section 3 we present the model, with additional details in the appendix. Finally, in sections 4 and 5 we present the results and conclusions.

2. Experimental setup

In the experiment, a 100-μm thick, 8-at. % Yb-doped disk with a nominal cold radius of curvature of -3.84 m bonded onto a diamond heat sink (TRUMPF Scientific Lasers) is used. The disk is placed into a commercial 44-pass thin-disk head (TRUMPF Scientific Lasers) and pumped with a free-space-coupled laser diode. Pumping is performed into the 940-nm absorption band. Note, the multimode pump beam has an octagonal shape due to the homogenizer placed in between the pump diodes and thin-disk head. A schematic of the experimental setup is shown in Fig. 1(a). The convex mirror has a nominal radius of curvature of 2 m. An output coupler (OC) with a

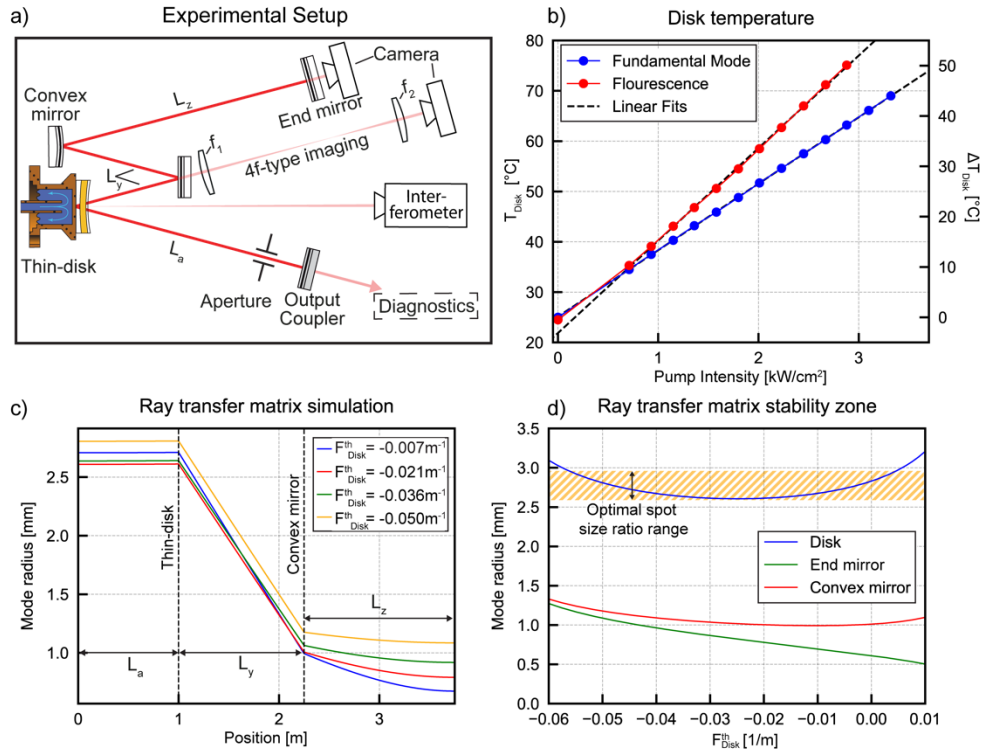transmission rate of 10.2% is used, the angle of incidence on the thin-disk is chosen to be about 5°.

Fig. 1. (a) Schematic of the concave-convex thin-disk laser cavity used for the experiments. The water cooled thin-disk is the concave element of the cavity and a convex mirror is introduced in one arm. The intracavity laser beam at the end of the cavity and at the disk is monitored through the residual transmission using a pair of cameras which are both equipped with 1000 nm long-pass filters (Thorlabs FELH1000) to filter out scattered pump light. Additionally, a 4f-type-imaging scheme ($f_1 = 300$ mm, $f_2 = 150$ mm) is used in case of the beam on the disk. An interferometer can be used to measure the surface profile of the thin-disk during fluorescence or laser operation. (b) Disk temperature measurement in fluorescence (blue) and fundamental mode lasing (red) with linear fits for $I_{pump}>0$. (c) Conventional ray transfer matrix cavity simulation for different indicated thermal lens values of the thin-disk (F_{disk}^{th}) showing the mode radius evolution across the cavity. The relevant arm lengths are marked L_a, L_y, L_z. (d) Ray transfer matrix simulation predicted mode radius on the thin-disk (blue), end mirror (green) and convex mirror (red). The shaded region indicates the 70% - 80% ratio between laser and pump radii, which is the empirically-found range where fundamental lasing is typically achieved in TDLs.

The setup allows for the imaging of the intracavity beam at different points of the resonator by utilizing the residual transmission through the highly reflective mirrors which are placed in low-distortion mirror mounts. To monitor the intracavity beam at the position of the disk in the resonator, a 4f-type-imaging setup (using two lenses with different focal lengths and accordingly adjusted lengths) is employed. An aperture can be introduced into the cavity. During the experiment, the arm lengths of the resonator, L_a, L_y, L_z are varied to scan a wide parameter space of oscillator configurations. The laser is operated inside an air environment. A thermal camera (FLIR) is used to measure the temperature of the thin-disk and a Twymann-Green interferometer (TRIOPTICS µPhase-500 operating at 632.8 nm) can be installed to measure the

surface profile of the thin disk under operating conditions. Both the thermal camera measurement and the interferometer measurement can be performed during fluorescence operation (pumped gain medium without lasing) and laser operation. The relation between disk temperature and pump intensity is shown in Fig. 1(b). Bending of the disk is expected to depend primarily on disk temperature, so temperature is a useful quantity to enable comparison between fluorescence and lasing modes of operation [15]. For each laser configuration, the M^2 beam quality parameter (Thorlabs BP104-IR) and the output power (Coherent LM-5000) are measured. Using conventional ray transfer matrix simulation, the mode radius evolution inside the cavity can be initially predicted (Fig. 1(c)). The resulting stability zone due to the ray transfer matrix simulation suggests that this laser will operate in the optimal operation range over a relatively large range of thermal lensing up to $-0.06/m$ as indicated in Fig. 1(d).

Figure 2 shows the measured beam profiles at different pump intensities for an example cavity with arm lengths $L_a = 1000\,mm$, $L_b = 1250\,mm$, $L_c = 1500\,mm$. Depending on the operating point, the laser can exhibit triangularly-shaped distortions (Fig. 2(a)), Gaussian modes (Fig. 2(b)) or higher order modes (Fig. 2(c)). To understand the observed behavior, the surface profile of the disk is measured interferometrically.
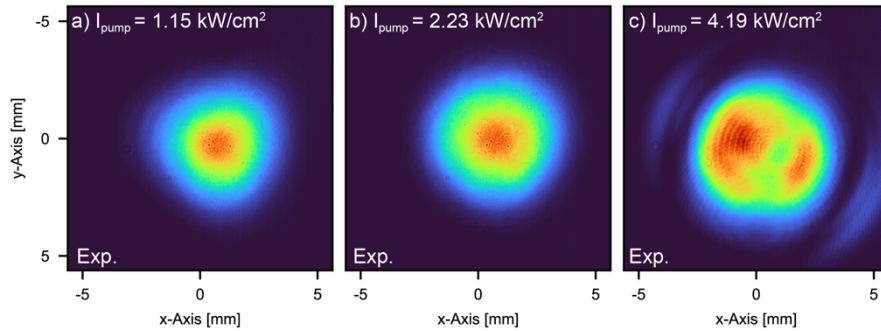

Fig. 2. Measured intracavity beam profiles imaged at the location of the thin-disk. The arm lengths are chosen to be $L_a = 1000\,mm$, $L_y = 1250\,mm$, $L_z = 1500\,mm$. The pump intensities are indicated.

The reconstructed surface profile of the disk is shown in Fig. 3. The reconstruction is done with a fixed radius for the analysis of 8.2 mm by extracting all Zernike polynomials of order up to $n + |m| \leq 6$ from the interferometric measurement. In Figs. 3(c),(d) the first four Zernike polynomials (corresponding to piston, tilt, and parabolic deformation) are set to zero to illustrate the non-parabolic surface deviation of the disk. While the disk is almost parabolic (to $\pm 40\,nm$ across the 7.4 mm pump spot, corresponding to a deviation $<\lambda/20$) there are clearly non-rotationally symmetric aberrations present. These can be seen to exhibit threefold symmetry, especially at the edges of the disk. As we will show in the following, this threefold symmetry is responsible for the triangularly distorted fundamental modes in Fig. 2(a). These non-rotationally symmetric surface profile features are attributed to the thin-disk mounting [26].

By measuring the disk surface at several disk temperatures T_{Disk}, we obtain approximate temperature-dependent Zernike coefficients $c_n^m(T_{Disk})$ as a function of disk temperature. Together with a measured relation between the pump intensity I_{pump} and disk temperature, this provides an analytical description of the disk surface profile, and thus the phase profile imprinted onto the intracavity laser beam each time it is reflected by the disk.
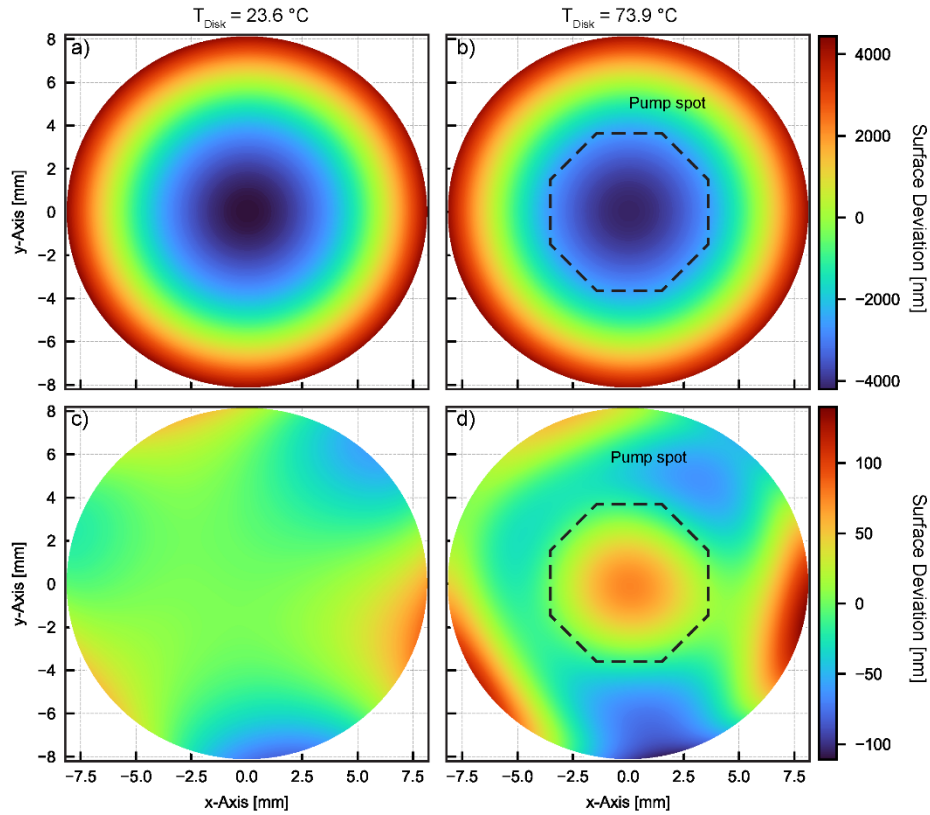
Fig. 3. Reconstructed surface profile using Zernike polynomials up to n + |m| ≤ 6 of the disk used in our experiment based on interferometric measurements using a Twymann-Green interferometer. The full surface profile is shown for two cases: (a) in the un-pumped state, and (b) in the optically pumped state but without lasing (fluorescence mode). The corresponding non-parabolic parts are shown for the unpumped state (c) and optically pumped state (d). The non-rotationally symmetric phase distortions are clearly visible in both cases. In (b) and (d) the size and position of the octagonal pump spot is indicated.

3. Cavity model

The aim of the cavity simulation presented here is to provide a thorough model considering as many effects as possible that can influence the laser operation while not depending on many assumptions and keeping the calculations relatively efficient. Continuous-wave and linearly polarized beams are assumed. Importantly, the spatially resolved measured surface profile of the thin disk shown in Fig. 3 is included.

3.1. Theory

The simulation finds a steady-state electric field distribution inside the optical resonator by propagating the electric field over many resonator roundtrips until the field distribution converges. Here, the number of simulated roundtrips is much larger than the cavity lifetime. The cavity is simulated in a split-step approach: each cavity element is applied to the electric field in real space and the free-space propagation between the cavity elements is applied in reciprocal space. At each cavity element, a spatially resolved and in principle arbitrary phase profile and gain profile are applied. This enables us to account for even the most complex cavity elements. More

details on this can be found in Appendix A. This model enables a detailed description of cavities away from the approximation of parabolic phases which allows a careful look into optimizing the output beam quality of high-power TDLs. Due to an accurate model for the disk gain, the model also provides an absolute prediction of the average output power.

3.2. Implementation

First, a discretization onto a grid of points of size n × n, here with n = 2^9 = 512 points, is performed. This grid needs to be chosen fine enough that even high frequency components of the computed electric field can be represented with sufficient resolution. Simultaneously, the total size of the simulated area needs to be chosen large enough, such that the entire cavity mode can be captured on every cavity element, here it is chosen to be 30 mm × 30 mm. At every cavity element, it is assumed that the amplitude and phase profile can be applied to each grid point independently and that there is no interaction between different grid points.

An accurate description of the laser gain is crucial to the simulation. Not only is the correct absolute gain value essential for output power prediction, but also the gain distribution shaped by pump and laser intensity play an important role in the shaping of the cavity mode that is not captured by ray transfer matrix analysis. We approximate the Yb-doped gain medium via the standard rate equation model for quasi-three-level lasers, with wavelength dependent effective emission and absorption cross sections (see Eq. (7) in Appendix A). The rate equations are solved in the plane of the disk. Inserting the volume number density of the doping ions and the photon fluxes of the optical pump and the laser, the inversion of the laser gain medium in the steady-state is computed. The multiple passes of laser and pump beams are accounted for (see Appendix A.3). Temperature dependent absorption and emission cross sections are taken from [27]. These are supplied to the simulation at the desired disk temperature with the assumption of constant disk temperature across the pump spot. The gain distribution of the pump spot is approximated with a supergaussian of order 6 of octagonal shape. This results in a spatially resolved amplitude profile of the gain that can be applied to the electric field as described above. The phase profile of the disk is computed from interferometer measurements such as those shown in Fig. 3.

Example amplitude gain profiles that are applied to the electric field on each disk pass are shown in Figs. 4(a)-(c) where the depletion due to the laser intensity distribution can clearly be seen. Corresponding intensity distributions of the simulated laser mode at the location of the disk are shown in Figs. 4(d)-(f). These correspond to the same cavity and pump power as the experimentally measured beam profiles in Fig. 2, showing a good quantitative agreement between the model and experiments.

An algorithm for the acceleration of the convergence of the electric field distribution by essentially providing a better guess for the starting distribution of the electric field is also implemented and explained in Appendix A.5.

To verify that the simulation has successfully converged, we check that the predicted output power of the resonator does not change significantly in the last few simulated roundtrips (see Appendix A.5 for details). This takes care of identifying possible oscillating solutions of the simulation.

As arbitrary gain profiles can be included in the simulation, it is easy to also implement apertures, which was done here (see Fig. 1(a))
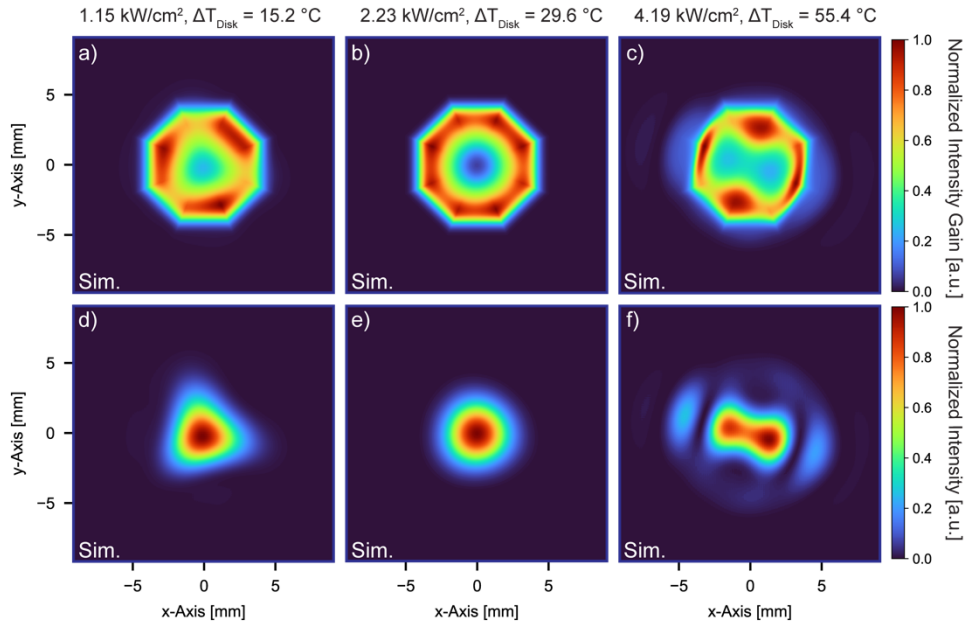
Fig. 4. Simulated gain profiles (normalized) and corresponding intensity distributions (normalized) for different resonator working points. The gain profiles are shown for triangular distorted fundamental mode operation (a), gaussian mode operation (b) and higher order mode coupling (c). Resulting intensity distribution on the thin disk are shown in (d)-(f). These simulations correspond to the experimentally measured cavity configurations shown in Fig. 2.

4.   Results and discussion

For the experimental validation of the described cavity simulation, a wide range of concave-convex cavities of the type shown in Fig. 1(a) are both simulated and experimentally realized by varying the arm lengths L_y and L_z. Close behind the output coupler an aperture with a diameter of 12 mm is installed. Of special interest are the cavities in which the simulation predicts modes away from Gaussian fundamental modes. This includes the case of distorted fundamental modes with trefoil symmetry, and the case of higher order modes. Both of these cases were seen initially in experiment as depicted in Fig. 2. For each cavity, a scan of the disk temperature T_{Disk} is carried out by varying the supplied pump power (relation of $T_{Disk}(I_{pump})$ depicted in Fig. 1(b)).

4.1.   Classification of output beams

As validation of the model, we categorize the laser operation into three distinct cases: fundamental Gaussian mode operation, distorted fundamental mode operation and operation with significant influence from high order modes. To classify operation with higher order mode contribution, we measure the beam quality parameter M^2 and higher order mode operation to be $M^2>1.3$. The same cutoff value is applied to the data obtained from simulations, where we compute the M^2 parameter from the predicted electric field at the output mirror.

Triangular output beam shapes are classified algorithmically. For this, we first compute the radius as a function of angle in polar coordinates. We then classify as triangular those beams that both have a sufficient modulation of the radius versus polar angle (i.e. have pronounced enough corners) and where the angular frequency component corresponding to threefold symmetry is largest. More detail and an example are provided in Appendix B.

4.2. Cavity scans

We carried out the cavity scans and perform the beam classification at the intracavity position of the disk as explained in section 4.1. This finally leads to areas that comprise a combination of certain arm lengths L_y and L_z and disk temperatures which produce triangular distorted fundamental mode beams or couple to higher order modes. These distinct regions are shown in Fig. 5 as a function of cavity length and disk temperature (which is varied by adjusting the pump power). For some combinations of arm lengths, both undesirable operations schemes are observed, e.g., triangular distorted mode beams at low power and coupling to higher order modes at higher powers.
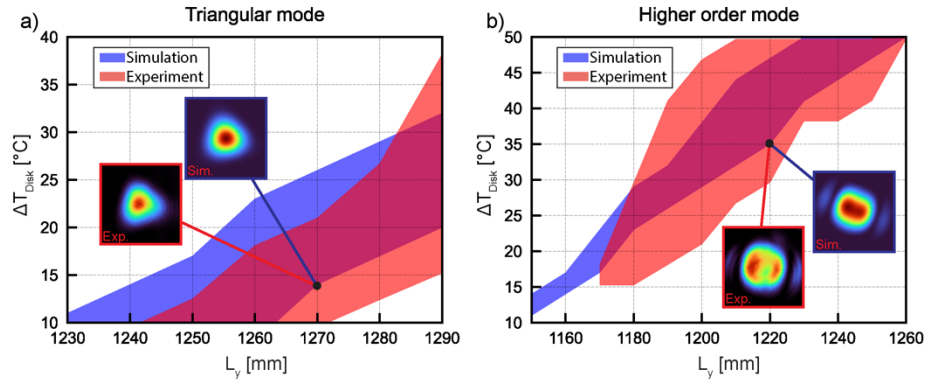

Fig. 5. Results of the spatially resolved cavity simulation and corresponding experiments. In (a) the shaded areas correspond to working points at which the indicated cavities exhibit a triangular distorted fundamental mode imaged at the location of the thin-disk classified according to section 4.1. In (b) the shaded areas correspondingly represent areas in which the beam quality degrades due to coupling to higher order modes and values of $M^2 > 1.3$ are observed either in experiment (red) or simulation (blue). The insets show example beam profiles of the simulated (blue border) and the experimentally observed (red border) cavities. Both figures show a scan of L_y keeping $L_a = 1000$ mm and $L_z = 1500$ mm constant while incrementing L_y in steps of 10 mm. The temperature is varied in steps of 3°C in simulation and experiment.

For the region in which triangular distorted fundamental modes are predicted, good agreement with experiment is found. The experimentally observed region for higher order mode beams seems to be centered well around the region of predicted higher-order mode beams, but in experiment this region is broader. This could be due to small-scale perturbations like slight thermal drift and off-centering of the laser beam on the disk, promoting coupling to higher order modes in a slightly larger parameter space than in the steady-state of the simulation which might also be influenced by an off-center aperture. Furthermore, in the regions with predicted triangular operation or higher-order mode coupling, the simulation usually predicts a worse beam quality value in the middle of these predicted zones. This is attributed to the assumed perfect centering of all elements in the simulation which cannot be achieved in experiment. Apart from the intentionally introduced aperture of 12 mm present in both experiment and simulation, further investigation showed that additional apertures that are large compared to beam size ($r_{ap} \gg 4 \cdot w_{laser}$) and placed slightly off-center can break the symmetry enough to suppress much of the very high order modes. This contributes to worse beam quality while not changing the range of predicted fundamental mode and higher-order mode operation significantly. In the experiment these large apertures are for example provided by mirrors while no mirror aperture is included in simulation.

To achieve the high level of agreement for triangular distorted beams shown in Fig. 5(a) special care had to be taken to not distort the cavity mirrors while mounting, and low-distortion mounts were used to ensure this. The slight shift between predicted and observed distorted fundamental mode regions still present is attributed to some residual aberrations that still occur on cavity elements other than the disk despite this low distortion mounting as well as due to the tolerances of the radii of curvatures of the used mirrors.

The output power is also predicted by the simulation as described above. Figure 6(a) shows a comparison between the simulated and experimental average output power as a function of pump power for an example cavity with $L_y = 1250$ mm; other cavity parameters were the same as in Fig. 5.
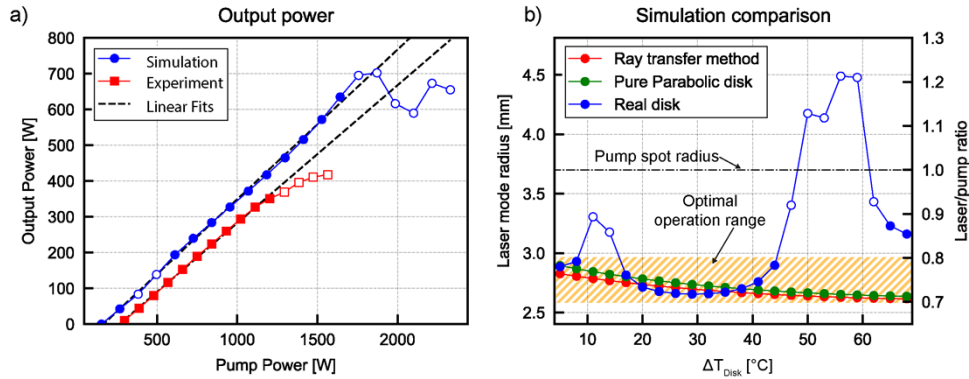

Fig. 6. (a) Laser output power predicted by the simulation (blue) and observed in experiment (red) for an example cavity with $L_a = 1000$ mm, $L_y = 1250$ mm and $L_z = 1500$ mm. Data points for which higher order mode operation with $M^2 > 1.3$ is simulated or observed are marked with non-filled data points. For both cases a linear fit to the fundamental lasing region with $M^2 < 1.3$ is performed (black, dashed). From these fits the slope efficiency is extracted. (b) Cavity mode size at the disk for the different simulations: The conventional ray transfer matrix formalism (blue), a spatially resolved model with only the parabolic part of the disk included (green) and the full model with the measured surface profile of the disk included (red). Hollow data points indicate $M^2 > 1.3$. The right vertical axis marks the relative laser spot size to pump spot size ratio. The often-provided empirical optimal operation range of $70\% - 80\%$ for TDLs is hatched orange.

In the range in Fig. 6(a) where the cavity exhibits near fundamental mode lasing in both simulation and experiment, an offset can be seen between the predicted and measured output powers of the resonator. This is effectively equivalent to a predicted lower pump laser threshold of 165 W than the observed threshold of 265 W. The slope efficiency of the cavity, however, is similar in both cases with a predicted value of 42% and a measured slope efficiency of 39% in the range up to 1.2 kW of pump power. These values are determined with a linear fit inside these regions as shown in Fig. 6(a). We mainly attribute the change in laser threshold and the slightly reduced slope efficiency to the uncertainty of the doping concentration in the laser crystal. Additionally, we neglected in our simulations small losses from other cavity elements and the thin-disk anti-reflection coating. The behavior of decreasing output power as higher-order modes are exited is also observed experimentally in near fundamental mode operation in straight (two-mirror) resonators [18].

The comparison of the full spatially resolved simulation to a conventional simulation using the ray transfer matrix formalism is shown in Fig. 6(b). For further comparison, the figure also shows the predictions of the spatially resolved model when only the parabolic part of the disk phase profile is included. This pure parabolic simulation shows good agreement with the ray

transfer matrix method, as is expected. The slight deviations in spot sizes between the two can be attributed to some coupling still being able to take place in the simulation despite the purely parabolic aberrations. Also, in the parabolic aberration simulation, the spatially resolved gain profile is included which is not the case for the ray transfer matrix simulation.

Comparing the full spatially resolved simulation to the two simplified cases clearly demonstrates the importance of the inclusion of non-rotationally symmetric, non-parabolic aberrations of the disk. It should also be noted that the contribution to beam distortions from including the spatially resolved gain distribution is much less than from the phase distortions. The expected operation range with well-behaved laser output shrinks considerably when taking these aberrations into account.

5. Conclusions

We present a detailed investigation into the influence of aberrations on output parameters of thin-disk oscillators. We show that seemingly small deviations from a perfect parabolic disk and especially non-rotationally symmetric aberrations have a very noticeable and sometimes detrimental impact on the laser mode and output power. We show a spatially resolved cavity simulation model that supports arbitrary, non-trivial surface profiles that is in good agreement with experiments. It thus becomes clear that even deviations of a perfect surface on the order of $\lambda/20$ across the pump spot, that might have been previously discounted as unimportant, must be considered in the design of high-power thin-disk oscillators. The new full spatially resolved model including spatially resolved phase and gain provides for the first time a detailed look into the influence of higher order aberrations of the thin disk, that can be introduced by contacting, clamping and thermal effects. Comparing the full simulation to the simpler ray transfer matrix model commonly used clearly demonstrates the importance of the inclusion of non-rotationally symmetric, non-parabolic aberrations of the disk, as this can reduce the predicted stability range of the oscillator considerably. These insights will be of great importance for cavity design and component assembly for kW-class high-power thin-disk oscillators, especially in multipass arrangements and when scaling the pump and mode size on the disk.

Furthermore, the model described here can be adapted to cover bulk solid-state lasers or to improve the performance of semiconductor disk lasers (also known as vertical external cavity surface emitting lasers, VECSELs) [28,29] in the future as the beam quality of these laser architectures are dependent on non-trivial surface profiles of cavity elements. This model can also directly be applied to laser amplifiers based on the thin-disk architecture since these can also be susceptible to similar mode degradation issues as those investigated here.

Appendix A. Computational implementation details

A.1 Non-flat cavity elements considering a non-zero angle of incidence

In the case of elements with perfect parabolic phase profiles, a non-zero angle of incidence θ on the element can be modeled as an effective radius of curvature of the element along and perpendicular to its plane of incidence, respectively [30]:

$$R_x = R\cos(\theta) \tag{1}$$

$$R_y = \frac{R}{\cos(\theta)}. \tag{2}$$

A similar effect can be expected for an angle of incidence on cavity elements which are defined by exact, non-parabolic phase profiles like the disk, but the handling becomes non-trivial. In general, a local radius of curvature can be extracted from an arbitrary phase profile by taking the

second derivative:

$$R_{\mathrm{j}}[\phi](x,y) = \frac{1}{\partial_{\mathrm{j}}^2 \phi(x,y)} \tag{3}$$

where $\phi(x,y)$ is the phase at the corresponding coordinates x, y. We chose to approximate the transformed phase profile under an angle of incidence θ with

$$\phi_\theta(x,y) = \phi\left(\frac{x}{\cos\theta}, y\right) \cos\theta. \tag{4}$$

This expression correctly reproduces the change in local radius of curvature found for spherical optics. It is analogous to a change of coordinates in the plane of incidence together with a projection of the wave vector along the surface normal of the optic.

A.2 Free space propagation

Free space propagation over a distance L is described in reciprocal space by a phase factor applied to each frequency component. Thus, the operator for free space beam propagation $\hat{S}_{\mathrm{freespace}}$ is given by:

$$\hat{S}_{\mathrm{freespace, L}}[E](x,y) = \mathcal{F}^{-1}\left[\mathcal{F}[E](k_{\mathrm{x}}, k_{\mathrm{y}}) \cdot e^{-i\sqrt{k^2 - k_{\mathrm{x}}^2 - k_{\mathrm{y}}^2}L}\right](x,y). \tag{5}$$

A.3 Three-level gain medium

To accurately capture gain saturation, the rate equations at each position of the simulation grid at the plane of the disk are solved. Here we assume that there is no influence between neighboring grid points. The gain of the disk g_{Disk} can thus be written as:

$$g_{\mathrm{Disk}}(x,y) = g_{\mathrm{Disk}}\left(I_{\mathrm{tot, pump}}(x,y), I_{\mathrm{tot, laser}}(x,y)\right), \tag{6}$$

where $I_{\mathrm{tot, pump}}(x,y)$ and $I_{\mathrm{tot, laser}}(x,y)$ are the pump and laser intensities at (x,y) added over all disk passes, respectively. In the absence of any higher order effects, Yb-doped gain materials can commonly be approximated by the quasi-three-level rate equations with effective emission and absorption asymmetric cross sections.

The effective rate equation for the upper state can be approximated as [31]:

$$\frac{dN_2}{dt} = -\gamma_{12}N_2 + \left[\left(\sigma_{\mathrm{abs}}^{\mathrm{p}}N_1 - \sigma_{\mathrm{em}}^{\mathrm{p}}N_2\right) \cdot \frac{I_{\mathrm{p}}}{h\nu_{\mathrm{p}}} + \left(\sigma_{\mathrm{abs}}^{\mathrm{l}}N_1 - \sigma_{\mathrm{em}}^{\mathrm{l}}N_2\right) \cdot \frac{I_{\mathrm{l}}}{h\nu_{\mathrm{l}}}\right], \tag{7}$$

where $N_{1,2}$ are the population densities of the lower and upper states of the Yb-doping ions, γ_{21} the decay rate of the upper state, $\sigma_{\mathrm{abs, em}}^{\mathrm{p,l}}$ the temperature-dependent absorption and emission cross sections at pump and laser frequencies. The photon energies are $h\nu_{\mathrm{p,l}}$ for pump (p) and laser (l). With the total volume number density $N_0 = N_1 + N_2$, the inversion $\beta = N_2/N_0$ and the photon fluxes $R_{\mathrm{p,l}} = \frac{I_{\mathrm{p,l}}}{h\nu_{\mathrm{p,l}}}$ the rate equation can be written as

$$\frac{\mathrm{d}\beta}{\mathrm{d}t} = \gamma_{12}\beta + \left[\left(\sigma_{\mathrm{abs}}^{\mathrm{p}}(1-\beta) - \sigma_{\mathrm{em}}^{\mathrm{p}}\beta\right)R_{\mathrm{p}} + \left(\sigma_{\mathrm{abs}}^{\mathrm{l}}(1-\beta) - \sigma_{\mathrm{em}}^{\mathrm{l}}\beta\right)R_{\mathrm{l}}\right]. \tag{8}$$

Note, the pump photon flux implicitly includes the multi-pass arrangement, with the total found by summing over all passes accounting for absorption experienced on each pass. Solving for the steady state $\frac{\mathrm{d}\beta}{\mathrm{d}t} = 0$, the expression for the inversion as a function of pump and laser fluxes

is obtained:

$$\beta = \frac{\sigma_{abs}^{p} R_p + \sigma_{abs}^{l} R_l}{\gamma_{12} + (\sigma_{abs}^{p} + \sigma_{em}^{p})R_p + (\sigma_{abs}^{l} + \sigma_{em}^{l})R_l}. \tag{9}$$

In general, the rate of change of a photon flux R in a medium with emission and absorption cross sections σ_{em} and σ_{abs} along the propagation axis z is given as:

$$\frac{dR}{dz} = RN_0(\sigma_{em}\beta - \sigma_{abs}(1 - \beta)). \tag{10}$$

In the case described here, the rate used is the implicitly summed rate over all reflections on the disk $R_{p,l}$, for pump and laser respectively.

Assuming constant inversion over the L = 100 μm thick disk, the single pass intensity gain for the disk is given as

$$G_j(\beta) = \exp(N_0(\sigma_{em}^{p,l}\beta - \sigma_{abs}^{p,l}(1 - \beta))L). \tag{11}$$

As can be seen from the equations above, the inversion β depends on the photon fluxes $R_{p,l}$, which in turn depend on the single pass gain, which again depends on the inversion. Thus, this system of equations cannot be solved analytically, but is straightforward to solve numerically for the inversion given the input photon fluxes of laser and pump. From this finally the spatially resolved amplitude factor of the disk can be computed as:

$$g_{Disk}(x, y) = \sqrt{G_l(\beta(R_{0,p}(x, y), R_{0,l}(x, y)))}. \tag{12}$$

A.4 Cavity roundtrip simulation

The roundtrips of the cavity are simulated consecutively. The input for each roundtrip are the relevant electric fields from the previous roundtrip. These are given by the electric field E_{prev} at the end of the previous roundtrip, as well as the electric fields $[E_{disk,1}, \ldots, E_{disk,n}]$ for the passes of the laser on the disk. Here, n is the number of disk hits per roundtrip (n = 2 in the case of the cavity discussed in the body of the text).

At the beginning of each roundtrip the current electric field E_{curr} is stored in $E_{prev} \leftarrow E_{curr}$ for reference. Then, at each cavity element the current electric field is updated with the cavity element or freespace operator (Eq. (5)), respectively:

$$E_{curr} \leftarrow \hat{S}_{el/freespace}[E_{curr}]. \tag{13}$$

If the cavity element is the disk, the array of electric fields at the disk is updated with the current electric field by appending it to the list and removing the first element from it:

$$[E_{disk,1}, \ldots, E_{disk,n}] \leftarrow [E_{disk,2}, \ldots, E_{disk,n}, E_{curr}]. \tag{14}$$

Then the electric field is computed with the gain function introduced in Appendix A.3. For the laser intensities all electric fields of the last n passes on the disk (Eq. (14)) are considered:

$$E_{curr} \leftarrow g_{disk}\left(I_{tot, pump}, \left|\sum_{i=1}^{n} E_{disk,i}\right|^2\right) \exp(i\phi_{disk}) \cdot E_{curr}. \tag{15}$$

Here we note that the gain is recomputed every time the disk cavity element is reached. When all elements of the cavity roundtrip have been considered and applied to the electric field, the next cavity roundtrip is started with the updated electric field E_{curr} and the updated array of electric fields at the last n disk hits.

Finally, we note that the simulation does not include spatial hole burning or amplified spontaneous emission and assumes the laser to be perfectly monochromatic.

A.5 Convergence

Overall, the procedure explained in Appendix A.4 is carried out until the convergence of E_{curr} is reached. However, because the convergence of the simulation is sometimes relatively slow when the steady-state mode is far away from the initial guess, a convergence acceleration algorithm is implemented. If this is turned on, then for the first few hundred round trips an averaging procedure is applied to the electric field at the end of each roundtrip. Specifically, the electric field is averaged from one roundtrip to the next according to:

$$E_{avg} = E_{curr} + \alpha E_{prev} \cdot \exp\left(i \cdot \arg\left(\iint E_{curr} E_{prev}^* \mathrm{d}x\mathrm{d}y\right)\right). \tag{16}$$

Here, the factor α is attenuating the previous roundtrip so that they have an exponentially decreasing impact on the next roundtrip. The process can roughly be understood as a filter to suppress the weaker transverse modes which lead to an oscillation of the electric field distribution on the order of a few roundtrips. Finally, to preserve the total intensity from the original field E_{curr}, the current electric field is updated according to:

$$E_{curr} \leftarrow E_{avg} \frac{\iint |E_{curr}|^2}{\iint |E_{avg}|^2}. \tag{17}$$

Afterwards, the next roundtrip is started like described in Appendix A.4. After a few cavity lifetimes, the averaging process is switched off. In a final phase of the algorithm, a number of roundtrips larger than the cavity lifetime is simulated without averaging and it is verified that the solution converges. The convergence condition for the simulation is:

$$\sum_i \left|\frac{P_i}{P_{i-1}}\right| < 0.001 \tag{18}$$

where the sum runs over the last 10 roundtrips and P_i denotes the total power computed from the simulated electric field at the position of the output coupler in the i-th roundtrip.

Appendix B. Image classification

To correctly identify and distinguish the triangular distorted and Gaussian fundamental mode operation regimes of the laser an image classification on the beam shape is performed. An example of one such classification is provided in Fig. 7.
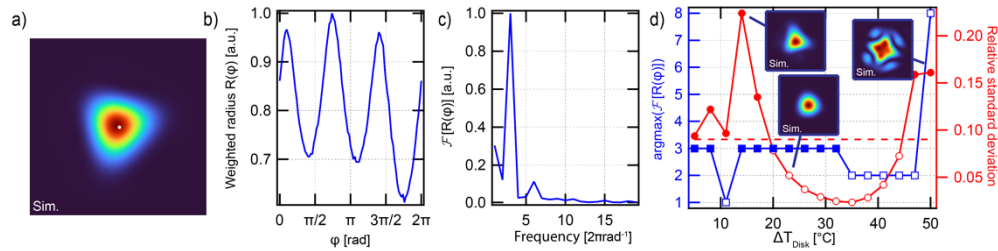

Fig. 7. Image classification algorithm example for a triangular beam. (a) Initial image with computed center of mass marked with white dot. (b) $1/e^2$ beam radius as a function of angle in polar coordinates. (c) Discrete Fourier transform of the angularly resolved beam radius. (d) Example of identification of the different regimes for the temperature scan of one cavity. The maximum contribution to the Fourier transform (blue) and the standard deviation of the angular resolved radius (red) are shown.

At first the center of mass (with respect to intensity, white dot in Fig. 7(a)) and the $1/e^2$ beam radius as a function of angle in polar coordinates is computed (Fig. 7(b)). A discrete Fourier transform of this angular resolved beam radius $r(\varphi)$ is subsequently performed (Fig. 7(c)). The first peak of the discrete Fourier transform is picked out to identify the periodicity of the beam, where a triangular beam shape will exhibit a periodicity of three. This is the first necessary condition for classification of a triangular beam. The second condition is that the relative standard deviation of $r(\varphi)$ must be greater than the cutoff-value defined at 0.09 to reject very weak triangular distortions (Fig. 7(d)).

Higher order mode operation is only defined by the measured M^2 value, where we define $M^2 > 1.3$ as having substantial contribution from higher-order modes.

Disclosures. The authors signed an NDA with TRUMPF with regards to the thin-disk module and head.

Data availability. Data underlying the results presented in this paper are not publicly available at this time but may be obtained from the authors upon reasonable request.

References

1. T. Südmeyer, S. Marchese, S. Hashimoto, C. Baer, G. Gingras, B. Witzel, and U. Keller, "Femtosecond laser oscillators for high-field science," Nat. Photonics **2**(10), 599–604 (2008).
2. S. Hädrich, J. Rothhardt, M. Krebs, S. Demmler, A. Klenke, A. Tünnermann, and J. Limpert, "Single-pass high harmonic generation at high repetition rate and photon flux," J. Phys. B: At., Mol. Opt. Phys. **49**(17), 172002 (2016).
3. L. L. Taylor, R. E. Scott, and J. Qiao, "Integrating two-temperature and classical heat accumulation models to predict femtosecond laser processing of silicon," Opt. Mater. Express **8**(3), 648–658 (2018).
4. P. Russbueldt, T. Mans, J. Weitenberg, H. Hoffmann, and R. Poprawe, "Compact diode-pumped 1.1 kW Yb: YAG Innoslab femtosecond amplifier," Opt. Lett. **35**(24), 4169–4171 (2010).
5. M. Müller, C. Aleshire, A. Klenke, E. Haddad, F. Légaré, A. Tünnermann, and J. Limpert, "10.4 kW coherently combined ultrafast fiber laser," Opt. Lett. **45**(11), 3083–3086 (2020).
6. A. Giesen, H. Hügel, A. Voss, K. Wittig, U. Brauch, and H. Opower, "Scalable concept for diode-pumped high-power solid-state lasers," Appl. Phys. B **58**(5), 365–372 (1994).
7. S. Nagel, B. Metzger, D. Bauer, J. Dominik, T. Gottwald, V. Kuhn, A. Killi, T. Dekorsy, and S.-S. Schad, "Thin-disk laser system operating above 10 kW at near fundamental mode beam quality," Opt. Lett. **46**(5), 965–968 (2021).
8. J. Dominik, M. Scharun, B. Dannecker, S. Nagel, T. Dekorsy, and D. Bauer, "Multi-kilowatt Ultrafast Laser with Thin-disk Technology," in *Laser Congress (ASSL,LAC)* (Optica Publishing Group, 2021).
9. C. J. Saraceno, F. Emaury, C. Schriber, A. Diebold, M. Hoffmann, M. Golling, T. Südmeyer, and U. Keller, "Toward Millijoule-Level High-Power Ultrafast Thin-Disk Oscillators," IEEE J. Sel. Top. Quantum Electron. **21**(1), 106–123 (2015).
10. C. J. Saraceno, D. Sutter, T. Metzger, and M. Abdou Ahmed, "The amazing progress of high-power ultrafast thin-disk lasers," J. Eur. Opt. Soc.-Rapid Publ. **15**(1), 15 (2019).
11. S. Nagel, B. Metzger, T. Gottwald, V. Kuhn, A. Killi, and S.-S. Schad, "Thin disk laser operating in fundamental mode up to a power of 4 kW," in *The European Conference on Lasers and Electro-Optics* (Optical Society of America 2019), pp. 4–5.
12. F. Saltarelli, I. J. Graumann, L. Lang, D. Bauer, C. R. Phillips, and U. Keller, "Power scaling of ultrafast oscillators: 350-W average-power sub-picosecond thin-disk laser," Opt. Express **27**(22), 31465–31474 (2019).
13. R. Paschotta, "Beam quality deterioration of lasers caused by intracavity beam distortions," Opt. Express **14**(13), 6069–6074 (2006).
14. A. Siegman, "Effects of small-scale phase perturbations on laser oscillator beam quality," IEEE J. Quantum Electron. **13**(5), 334–337 (1977).
15. A. Diebold, F. Saltarelli, I. Graumann, C. Saraceno, C. Phillips, and U. Keller, "Gas-lens effect in kW-class thin-disk lasers," Opt. Express **26**(10), 12648 (2018).
16. H. Kogelnik and T. Li, "Laser Beams and Resonators," Appl. Opt. **5**(10), 1550–1567 (1966).
17. V. Magni, "Multielement stable resonators containing a variable lens," J. Opt. Soc. Am. A **4**(10), 1962–1969 (1987).
18. Y. H. Peng, Y. X. Lim, J. Cheng, Y. Guo, Y. Y. Cheah, and K. S. Lai, "Near fundamental mode 1.1 kW Yb:YAG thin-disk laser," Opt. Lett. **38**(10), 1709–1711 (2013).
19. K. Schuhmann, K. Kirch, F. Nez, R. Pohl, and A. Antognini, "Thin-disk laser scaling limit due to thermal lens induced misalignment instability," Appl. Opt. **55**(32), 9022–9032 (2016).
20. A. Antognini, K. Schuhmann, and F. D. Amaro, *et al.*, "Thin-Disk Yb:YAG Oscillator-Amplifier Laser, ASE, and Effective Yb:YAG Lifetime," IEEE J. Quantum Electron. **45**(8), 993–1005 (2009).
21. T. Dietrich, C. Röcker, T. Graf, and M. Abdou Ahmed, "Modelling of natural convection in thin-disk lasers," Appl. Phys. B **126**(3), 47 (2020).

22. B. Weichelt, D. Blazquez-Sanchez, A. Austerschulte, A. Voss, T. Graf, and A. Killi, *Improving the Brightness of a Multi-kW Thin Disk Laser with a Single Disk by an Aspherical Phase-Front Correction* (SPIE, 2010).

23. J.-P. Negel, A. Loescher, A. Voss, D. Bauer, D. Sutter, A. Killi, M. A. Ahmed, and T. Graf, "Ultrafast thin-disk multipass laser amplifier delivering 1.4 kW (4.7 mJ, 1030 nm) average power converted to 820 W at 515 nm and 234 W at 343 nm," Opt. Express **23**(16), 21064–21077 (2015).

24. S. Piehler, B. Weichelt, A. Voss, M. A. Ahmed, and T. Graf, "Power scaling of fundamental-mode thin-disk lasers using intracavity deformable mirrors," Opt. Lett. **37**(24), 5033–5035 (2012).

25. S. Piehler, T. Dietrich, P. Wittmüss, O. Sawodny, M. A. Ahmed, and T. Graf, "Deformable mirrors for intra-cavity use in high-power thin-disk lasers," Opt. Express **25**(4), 4254–4267 (2017).

26. S.-S. Schad, A. Killi, V. Kuhn, and M. Graf, "Stress-optimized laser disk mounting systems," *U.S. patent* US10630038B2 (21 April 2020).

27. J. Koerner, C. Vorholt, H. Liebetrau, M. Kahle, D. Kloepfel, R. Seifert, J. Hein, and M. C. Kaluza, "Measurement of temperature-dependent absorption and emission spectra of Yb:YAG, Yb:LuAG, and Yb:CaF2 between 20 °C and 200 °C and predictions on their influence on laser performance," J. Opt. Soc. Am. B **29**(9), 2493–2502 (2012).

28. M. Guina, A. Rantamäki, and A. Härkönen, "Optically pumped VECSELs: review of technology and progress," J. Phys. D: Appl. Phys. **50**(38), 383001 (2017).

29. B. W. Tilma, M. Mangold, C. A. Zaugg, S. M. Link, D. Waldburger, A. Klenner, A. S. Mayer, E. Gini, M. Golling, and U. Keller, "Recent advances in ultrafast semiconductor disk lasers," Light: Sci. Appl. **4**(7), e310 (2015).

30. G. A. Massey and A. E. Siegman, "Reflection and Refraction of Gaussian Light Beams at Tilted Ellipsoidal Surfaces," Appl. Opt. **8**(5), 975–978 (1969).

31. R. Paschotta, J. Nilsson, A. C. Tropper, and D. C. Hanna, "Ytterbium-doped fiber amplifiers," IEEE J. Quantum Electron. **33**(7), 1049–1056 (1997).